Following the Olivine-Spinel Transition in Fayalite by Structure Refinements

J. Chen
SUNY, Stony Brook

Subduction processes are believed to bring $(Mg,Fe)_2SiO_4$ olivine, one of the most abundant minerals in Earth's upper mantle, to great depths, where its high pressure polymorphs, wadsleyite and ringwoodite (spinel structure), are stable. Mechanisms for the olivine-spinel transition and its effects on rheology are therefore important for understanding dynamic earth phenomena. Most of the previous studies on the transition have been carried out by examining samples recovered from high pressure and temperature, using transmission electron microscopy (TEM). Two different mechanisms are proposed for the olivine-spinel transition: (i) stacking fault and cation reordering(1) and (ii) diffusion-controlled nucleation and crystal growth(2). The first mechanism was supported by the TEM observation of a special orientation relationship between the olivine and spinel phase (e.g. $(100)_{Ol}$ is parallel to $(111)_{Sp}$) during the transformation(3, 4), and the second was suggested based by the absence of such an observation(4, 5). We have, for the first time, carried out a structure refinement study on the phase transformation in the iron-rich end member olivine (Fe_2SiO_4, fayalite) by using in-situ synchrotron x-ray diffraction data. The starting temperature of the phase transformation is found as low as 638 K. A two-step anion/cation ordering is observed and a significant deviatoric stress drop is detected at the transition.

The experiments were performed using the large anvil press SAM85 (6) at the X17B1 beamline at the NSLS. A recently developed translating imaging plate (TIP) diffraction system(7) was used to collect time-resolved x-ray diffraction patterns. The system takes advantage of the high energy and intensity of x-rays from the superconducting wiggler of X17. A monochromatic x-ray beam with 41.12 keV photon energy and 200 mm x 200 mm beam size penetrates a pressure medium made of boron and epoxy, then radiates the sample. Diffraction patterns are recorded on an imaging plate (IP) mounted on a translation stage. The translation axis is perpendicular to the incident x-rays in the horizontal plane. A lead screen is installed between the sample and the IP, with a vertical gap at the center to define the exposure area on the IP. The IP is translating during the exposure when the phase transformation proceeds so that all the changes in the diffraction from the sample are recorded during the transformation. We chose the iron-rich end member to investigate because it transforms into the spinel phase directly, without involving the diffusion process of the Mg-Fe chemical exchange. We compressed the powdered fayalite sample into the spinel stability field (6.9 GPa), then drove the olivine-spinel transition by increasing the temperature at a constant rate (0.03 K/sec). The spinel phase starts to appear at 638 K, and the transition is complete by 683 K, within about 25 minutes.

Eight diffraction patterns (integrated over 100 pixels on the imaging plate) of two coexisting phases were analyzed by Rietveld refinement. Figure 1 shows a typical result with 420 diffraction lines from two phases contributing to the pattern. The space group of the spinel phase is *Fd3m*; Z=8. For the standard origin at a center of symmetry, the three atoms in the asymmetric unit are Fe^{2+} at (1/2, 1/2, 1/2), Si at (1/8, 1/8, 1/8), and O at (*u, u, u*), with u~0.24. During preliminary refinements, the occupancies of all sites in the spinel phase are allowed to vary. This yields a full occupancy (1.0 to 1.1) for the oxygen site while the occupancies of Fe^{2+} cations at octahedral sites and Si^{4+} at tetrahedral sites are significantly below 1. In final refinements, the oxygen site is constrained at full occupancy, while the occupancies of the cation Fe^{2+} and Si^{4+}, together with lattice parameter, oxygen positional parameter, isotropic thermal parameters and phase fractions, are refined. Diffraction peaks of the olivine phase are significantly broadened due to deviatoric stress developed during the cold compression; the intensities are not sufficiently precise to derive accurate crystallographic data for the olivine phase in the presence of this

deviatoric stress. Results of the final refinements for the spinel phase are summarized in Table 1.

Occupancies of all the sites in the spinel structure *vs.* phase fraction of the spinel during the phase transition are plotted in Figure 2. The full occupancy of the oxygen site at the beginning of the transformation indicates that an ideal oxygen framework is formed when the phase transition starts. The tetrahedral (Si^{4+}) sites start with an occupancy of 69% in the first analyzed pattern, and become fully occupied faster than the octahedral (Fe^{2+}) sites which start with an occupancy of 74%. Although the structure refinement does not yield a full occupancy for the octahedral sites when the transition is completed, the R-factor (12.18%) yielded from this refinement is not significantly smaller than that (12.55%) from the refinement with a forced full occupancy for the octahedral sites. On the other hand, forcing full occupancies of tetrahedral and octahedral sites in the refinement at the beginning of the transition increases the R-factor from 9.98% to 12.99%. Therefore the cations can be considered less ordered at the beginning, and they gradually find their sites as the transition proceeds(8).

The changes in bond length and angle during the phase transition are listed in Table 2. The occupancy of Si^{4+} is the dominant factor over the occupancy of Fe^{2+} in controlling the bond length. Both O-O interatomic distances and Si-O bond length of the SiO_4 tetrahedral increase with increasing of the Si occupancy, and consequently O-O interatomic distances and Fe-O bond length of the FeO_6 octahedral decrease. When the tetrahedral sites are fully occupied, the occupancy of Fe^{2+} at the octahedral sites play the dominant role in controlling the bond length, and all the bonds change lengths in an opposite way with increasing of the Fe^{2+} occupancy.

Peak broadening of the diffraction pattern is analyzed to derive deviatoric stress of the sample for both the olivine and spinel phase. Differential strains of the sample can be evaluated by deconvolving the peak-width of the non-stressed sample(9). The result is plotted in Figure 3. Large differential strain in the olivine phase is introduced by the deviatoric stress developed during the cold compression. The differential strain is held in the olivine phase until the phase transformation. The spinel phase forms with very little differential strain; more than 80% of the total strain in the sample is released during the phase transformation.

Furthermore, the phase transition is very stress dependent. In a separate experiment, the sample is

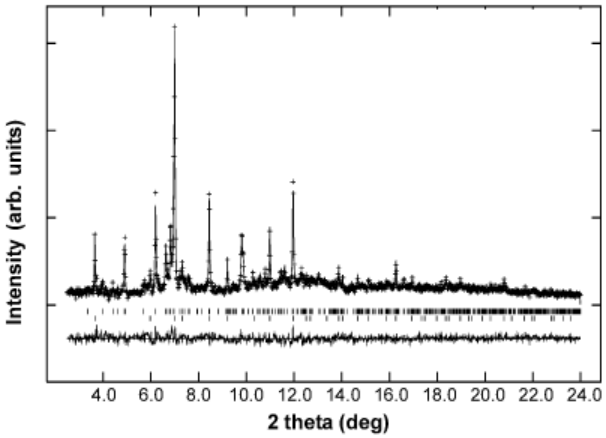

Figure 1. Structure refinement for two coexisting phases during the olivine-spinel phase transformation. The calculated and observed intensities are represented by a continuous line and crosses, respectively. A difference curve ($I_{obs} - I_{cal}$) is plotted at the bottom on the same scale. The olivine and spinel allowed reflection positions are indicated, respectively, by the first and second row of vertical bars.

Table 1
Result of the structure refinements for spinel during the olivine-spinel phase transformation

T(K)	a(Å)	V(Å^3)	u	F*(Si)	F*(Fe)	Ph†	R‡(%)	U(Si)(Å^2)	U(Fe)(Å^2)	U(O)(Å^2)
643	8.1834(4)	548.03(4)	0.2416(12)	0.69(5)	0.74(5)	0.18	9.98	0.005(2)	0.016(2)	0.040(1)
648	8.1853(2)	548.42(3)	0.2425(9)	0.87(4)	0.85(3)	0.29	9.53	0.007(4)	0.018(2)	0.024(4)
653	8.1872(2)	548.78(2)	0.2424(7)	0.94(3)	0.90(2)	0.46	10.40	0.012(3)	0.015(1)	0.017(4)
658	8.1880(2)	548.94(2)	0.2445(6)	1.00(3)	0.90(2)	0.65	11.01	0.018(2)	0.018(1)	0.025(3)
663	8.1890(1)	549.15(2)	0.2431(7)	1	0.91(1)	0.72	10.91	0.017(2)	0.019(1)	0.027(3)
668	8.1938(1)	550.12(1)	0.2418(6)	1	0.95(1)	0.85	11.84	0.018(2)	0.020(1)	0.022(3)
673	8.1948(2)	550.31(2)	0.2416(6)	1	0.94(1)	0.91	12.12	0.020(2)	0.020(1)	0.018(2)
683	8.1953(2)	550.41(3)	0.2418(6)	1	0.94(1)	1	12.18	0.020(2)	0.017(1)	0.018(3)

F: site occupancy. The integer 1 indicates that the site is constrained at full occupancy in the refinement.
† Ph: spinel phase fraction in the sample.
‡ $R = \Sigma | I_{obs} - I_{cal} | / \Sigma I_{obs}$

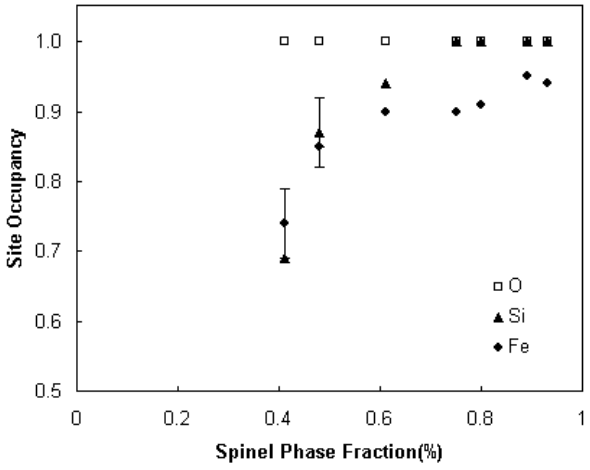

Figure 2. Site occupancies in spinel during the olivine-spinel transformation. Bars on the symbols indicate the experimental uncertainties.

Table 2
Changes of the tetrahedron and octahedron in spinel during the olivine-spinel phase transformation

Ph	F(Si)	F(Fe)	Si-O(Å)	O-O(Å)	V(t)(Å^3)	Fe-O(Å)	O-O(Å) shared	O-O(Å) Unshared	O-Fe-O(^{o})	O-Fe-O(^{o})	V(o)(Å^3)
0.179	0.69(5)	0.74(5)	1.65(2)	2.699(9)	2.317	2.116(10)	3.088(5)	2.897(4)	93.6(5)	86.4(5)	12.566
0.294	0.87(4)	0.85(3)	1.67(1)	2.721(8)	2.372	2.109(8)	3.067(3)	2.895(3)	93.3(4)	86.7(4)	12.452
0.464	0.94(3)	0.90(2)	1.67(1)	2.719(6)	2.368	2.111(6)	3.070(2)	2.898(2)	93.3(3)	86.7(3)	12.475
0.648	1.00(3)	0.90(2)	1.69(1)	2.766(6)	2.498	2.093(5)	3.023(2)	2.896(2)	92.5(3)	87.5(3)	12.191
0.718	1	0.91(1)	1.68(1)	2.735(6)	2.412	2.105(6)	3.055(2)	2.897(2)	93.0(3)	87.0(3)	12.387
0.852	1	0.95(1)	1.66(1)	2.708(6)	2.338	2.118(5)	3.087(2)	2.901(2)	93.6(2)	86.4(2)	12.587
0.913	1	0.94(1)	1.66(1)	2.703(6)	2.326	2.119(5)	3.090(2)	2.900(2)	93.6(2)	86.4(2)	12.619
1	1	0.94(1)	1.66(1)	2.708(6)	2.339	2.118(5)	3.088(2)	2.900(2)	93.6(3)	86.4(3)	12.594

pre-annealed in the olivine stability field (3 GPa); and consequently the olivine phase only contains about 0.2% deviatoric strain before the phase transformation. Two significant changes in the transition are observed: 1) the transition starting temperature is 100 K higher than the previous experiment; 2) the temperature range of the transition (two phase co-existing) is about twice as wide as the previous experiment.

The olivine-spinel phase transformation has been considered to be related to the origin of deep focus earthquakes through the transformational faulting hypothesis since a shear instability was found in samples which underwent the olivine-spinel phase transition(10, 11). This model holds only if a significant metastable olivine wedge exists in the subducting slab between 410 km and 660 km. This requires the temperature in the cold core of the slab to be low enough to kinetically inhibit the equilibrium transformation. The transition temperature observed in our experiment for fayalite is far below the believed cold slab temperature. Therefore, the existence of metastable olivine in the slab appears to be impossible. In a similar experiment with natural olivine, we have observed the olivine-spinel transformation at a temperature as low as 820 K. This transition temperature requires a slab thermal parameter (age * velocity) larger than 10,000 km for the metastable olivine wedge to extend down to 660 km(12). However, deep earthquakes which occur at this depth may have a thermal parameter as small as 6,000 km(11). Studies on recent large deep earthquakes, e.g. 1994 deep Tonga(13) and Bolivia(14) events, indicate that the earthquake fault plane is much wider than the assumed metastable olivine wedge. The transformational faulting model seems unlikely to be the origin of deep focus earthquakes.

On the other hand, our laboratory observation shows that this phase transformation releases the stress stored in the sample. Therefore, the earthquake driving force, stress, has to be generated and accumulated to high enough levels before the mineral transforms to a higher pressure phase. Weidner et al.(15) suggest that the stress capacity of olivine and its high pressure polymorphs is responsible for the bimodal distribution of deep focus earthquakes. A recent high pressure and temperature study on the strength of olivine, wadsleyite and ringwoodite shows that the olivine phase becomes very weak at temperatures above 700 K, while the ringwoodite remains much stronger at this temperature(16). Wadsleyite behaves rheologically between olivine and ringwoodite; stress relaxation in wadsleyite

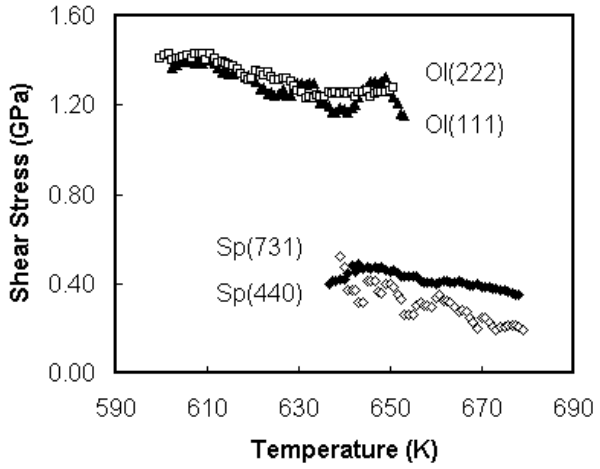

Figure 3. Shear stress in olivine (Ol) and spinel (Sp) phases. Different symbols indicate different diffraction lines used to derive the stress.

is slow at low temperatures like ringwoodite and fast at high temperatures like olivine. Therefore, a maximum stress can be expected at the depth where ringwoodite is stable. The bimodal distribution of deep focus earthquakes fits this stress profile.

Contributors to this work also include D. J. Weidner, J. B. Parise, M. T. Vaughan, and P. Raterron. The work was supported by the Center for High Pressure Research, an NSF Science and Technology Center, and the NSF grant EAR9909413.

References:

1. J.P. Poirier, in *Anelasticity in the Earth* F. D. Stacey, M. S. Paterson, A. Nicholas, Eds. (American Geophysical Union/Geological Society of America, Washinton D.C./ Boulder, Colorado, 1981), vol. 4, pp. 113 - 117.
2. C.-M. Sung, R. Burns, *Tectonophysics* **31**, 1 - 32 (1976).
3. A. Lacam, M. Madon, J.P. poirier, *Nature* **288**, 155 - 157 (1980); J.N. Boland, L.-g. Liu, *Nature* **303**, 233 - 235 (1983).
4. P.C. Burnley, H.W. Green(II), *Nature* **338**, 753 - 756 (1989).
5. P.J. Vaughan, H.W.C. II, R.S. Coe, *Nature* **298**, 357 -358 (1982); J. N. Boland, R. Liebermann, *Geophysical Research Letters* **10**, 87 - 90 (1983).
6. D.J. Weidner *et al.*, in *High-pressure research: Application to Earth and Planetary Sciences* Y. Synono, M.H. Manghnani, Eds. (Terra Scientific Publishing Company / AGU, Tokyo / Washington, D.C., 1992) pp. 13 - 17.
7. J. Chen *et al.*, *Review of High Pressure Science and Technology* **7**, 272 - 274 (1998).
8. M.D. Furnish, W.A. Bassett, *Journal of Geophysical Research* **88**, 10,333 - 10,341 (1983).
9. D.J. Weidner, Y. Wang, M.T. Vaughan, *Geophysical Research Letters* **21**, 753 - 756 (1994).
10. H. Green, H. Houston, *Annual Review of Earth and Planetary Science* **23**, 169 - 213 (1995).
11. S. Kirby, S. Stein, E. Okal, D. Rubie, *Reviews of Geophysics* **34**, 261 - 306 (1996).
12. J.P. Devaux, G. Schubert, C. Anderson, *J. Geophys. Res.* **102**, 24,627 - 24,637 (1997).
13. D.A. Wiens *et al.*, *Nature* **372**, 540 - 543 (1995).
14. P. Silver *et al.*, *Science* **268**, 69 -73 (1995).
15. J.D. Weidner, J. Chen, Y. Wu, Y. Xu, *EOS, Transactions, AGU* **79**, 915 (1998).
16. J. Chen, T. Inoue, D. Weidner, Y. Wu, M. Vaughan, *Geophysical Research Letters* **25**, 575 - 578 (1998).

Evidence from pyrrhotite compositions of different formation environments for interplanetary dust particles and carbonaceous meteorites

G. Flynn[1], A. Lanzirotti[2], and S. Sutton[3]
[1]State University of New York-Plattsburgh, [2]University of Chicago, [3]University of Chicago

Interplanetary dust particles (IDPs), which are typically ~10 microns in size, have been collected by NASA from the Earth's stratosphere since the mid-1970s. Although every solar system object is a potential source of IDPs, the detection, by the Infrared Astronomical Satellite, of dust trails or bands associated with the asteroid belt and with active comets indicates that the IDPs predominantly sample asteroids and comets. Both comets and the most primitive asteroids are believed to preserve, in relatively unmodified form, the dust out of which our Solar System formed. Thus, the composition and mineralogy of the primitive IDPs can provide direct information on the processes and conditions for dust formation early in the history of the Solar System.

The largest group of IDPs, called chondritic IDPs, is very similar in major element content to the most common meteorites, the chondritic meteorites. Based on their compositions and mineralogies, the chondritic meteorites sample parent bodies that never underwent differentiation, the process by which large bodies sepa-

rate into a Fe-rich core and a silicate-rich mantle. Among the chondritic meteorites, there is a correlation between the degree of primitiveness and the volatile element content, with the meteorites having higher volatile contents having experienced a lesser degree of thermal processing and alteration. The most volatile-rich type of chondritic meteorite, the CI carbonaceous chondrite type, has a chemical composition similar to that of the solar photosphere. These CI carbonaceous chondrite meteorites have long been accepted as the best samples of primitive solar system matter available for laboratory study. However, in prior measurements using the X-Ray Microprobe at X26A, we determined that the chondritic IDPs are enriched in the moderately volatile elements (Mn, Cu, Zn, Ga, Ge, and Se) by a factor of ~3 over the average composition of the CI carbonaceous chondrite meteorites [1]. This suggests the IDPs and the CI carbonaceous chondrite meteorites formed in different environments. The previously observed correlation, in chondritic meteorites, of volatile content with degree of primitiveness suggests that these IDPs are more primitive, that is they better preserve the record of early Solar System processes, than any known meteorite. Other investigators have reached the same conclusion based on the unequilibrated mineralogy and the preservation of large deuterium and ^{15}N anomalies in many IDPs.

However, individual IDPs weigh only a few nanograms and may sample different sources, thus many IDPs must be analyzed to provide a meaningful average composition. The comparison of single, identifiable minerals from the IDPs and from the CI chondritic meteorites may provide a more straightforward test of the origins of these materials. Some single mineral grains, particularly Fe-sulfides, are found on the IDP collectors and in chondritic meteorites. Selenium and sulfur have very similar chemical behavior. In primitive chondritic meteorites Se is the most S-following element, being hosted exclusively in the sulfides — pyrrhotite, pentlandite, troilite, and cubanite [2]. Thus, the Se/S ratio in the sulfide minerals is likely to reflect that ratio at the time and location of sulfide formation. A comparison of the Se contents in sulfides from IDPs with sulfides from CI carbonaceous chondrite meteorites should indicate if the sulfides in these two materials formed under the same conditions.

The Cosmic Dust Curatorial Facility at the NASA Johnson Space Center (JSC) performs a preliminary characterization, including acquisition of an Energy Dispersive X-ray (EDX) fluorescence spectrum, of each IDP before it is made available for study. The particles on the stratospheric collectors range from chondritic in composition, with an EDX spectrum dominated by Si and Fe but containing detectable Mg, Al, S, Ni, and sometimes Ca, through chondritic with significant sulfide, dominated by S and Fe but containing significant Si, Mg, Al and Ni peaks, to an almost pure Fe-sulfide, dominated by Fe and S with a minimal Si peak. Each IDP decelerates from an atmospheric entry velocity >11 km/sec (Earth escape velocity) by interaction with the Earth's atmosphere. Energy dissipation occurs mainly by heating, and the peak temperature reached by an IDP increases with particle entry velocity, density, and size. The high density (~4.6 gm/cc) of the Fe-sulfide IDPs compared to the mean density of ~1 gm/cc for the chondritic IDPs [3] results in more severe entry heating for the Fe-sulfide particles than the chondritic IDPs. The Fe-sulfide particles span a range of morphologies from sharp, hexagonal crystals, through crystals with rounded edges, and finally melted spheres. Pulse heating of sulfides from the Orgueil carbonaceous meteorite causes a loss of S and Se relative to Fe [4], so we have confined our comparison of IDP sulfides with CI meteorite sulfides to only well-formed, hexagonal pyrrhotite from the IDP collectors.

The NASA JSC Curatorial Facility allocated to us five well-formed, hexagonal particles whose EDX spectra were dominated by S and Fe. The five particles, one of which is shown in Figure 1, range from 10 to 25 micrometers in size. The small size of an individual IDP necessitates the use of state-of-the-art analytical instruments to obtain chemical and mineralogical measurements. At beamline X26A, x-rays from an NSLS bending magnet pass through a monochromator and are focused to an ~15 micrometer diameter beam spot using Kirkpatrick-Baez focusing mirrors [5]. The ~10 micron IDPs are well matched to the size of this analysis beam. We have used the X-Ray Microprobe at X26A to determine the chemical compositions using x-ray fluorescence and mineralogy using x-ray diffraction on individual IDPs.

We used a Brucker SMART 1000 CCD system installed on Beamline X26A to perform x-ray diffraction analyses of these Fe-sulfide IDPs. This Brucker system is optimized for collection of data out to high 2-theta angles, and on very weakly diffracting samples. For the purposes of these analyses the IDPs were not rotated during the acquisition of the x-ray diffraction data. Because of the spatially collimated beam at X26A, a few 'larger' particles that approach the diameter of the spot size (10 microns) may yield single diffracting points, dependant on crystal orientation relative to the orientation of the incident beam, while fine grained crystals (i.e. much smaller than the diameter of the incident beam) exhibit no preferred orientation and yield good powder diffraction patterns. With a number of careful analyses in a variety of orientations it is then possible to use this data to quantitatively determine the mineralogy of each of the IDPs.

For the x-ray fluorescence measurements, an ~16.5 Kev monochromatic x-ray beam was used for excitation, and the fluorescence x-rays were detected using a Canberra Si(Li) EDX detector. Under these analysis conditions, the detection limit is a few parts per million for the elements from Cu through Br in the IDPs. We also measured the chemical compositions of 20 pyrrhotite crystals, each 30 to 50 microns in diameter, that were hand-selected from an ~2 mm fragment of the CI carbonaceous chondrite meteorite Orgueil that had been crushed between two glass slides [4]. Each of these grains was a well-formed, euhedral pyrrhotite. Major elements were measured by electron-beam EDX analysis, and the trace elements were measured using the X-Ray Microprobe. We measured the Ni, Cu, Zn, Ga, Ge, and Se to Fe ratios, and inferred the concentrations of these elements using the Fe content of each pyrrhotite determined in the EDX analysis. To determine if the Orgueil pyrrhotites are representative of the pyrrhotites from the entire class of CI carbonaceous chondrites we also measured the trace element to Fe ratios of 26 pyrrhotites hand-selected from the CI meteorite Alais.

The major element EDX analyses of the 20 pyrrhotites from the Orgueil carbonaceous chondrite showed that:

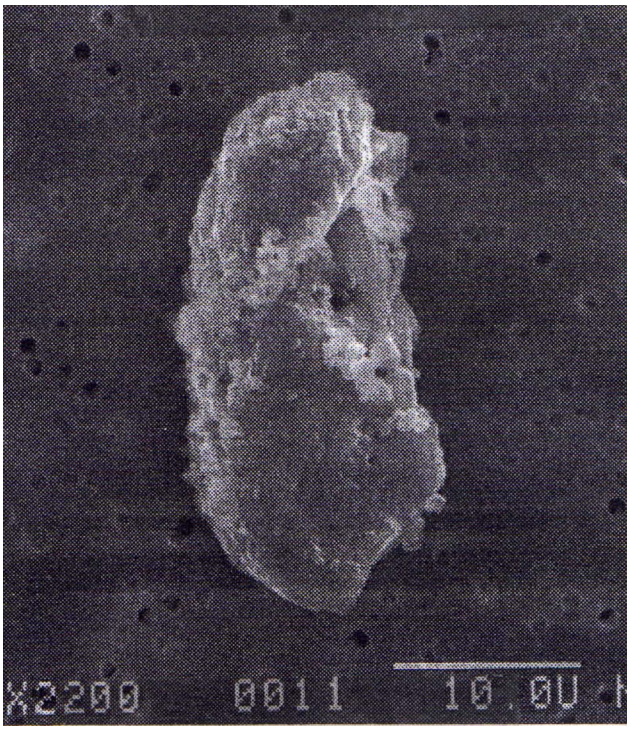

Figure 1. Scanning Electron Microscope image of a hexagonal pyrrhotite IDP, L2021D8.

Fe varied from 43.6 wt-% to 55.7 wt-%, with a mean of 50.2 wt-%,

S varied from 42.7 wt-% to 55.4 wt-%, with a mean of 48.3 wt-%, and,

Ni varied from 0.9 wt-% to 1.7 wt-%, with a mean of 1.4 wt-%.

The Fe and Ni contents showed variations of about 5% from their respective mean values, but the Ni content varied by as much as 40% from the mean. The mean Se content determined from the X-ray Microprobe analyses was 65 ppm, with a range from 36 to 100 ppm.

Major element EDX measurements have not been completed on the 26 pyrrhotites from the Alais CI carbonaceous chondrite meteorite, but the Se/Fe ratios showed approximately the same range as the pyrrhotites from Orgueil. If we assume each of the 26 Alais pyrrhotites has an Fe content of 50.2 wt-%, the mean of the Orgueil pyrrhotites, then the Alais pyrrhotites have a mean Se content of 76 ppm, compared to a mean of 65 ppm for the Orgueil pyrrhotites. The Se content of these Alais pyrrhotites ranged from 49 to 167 ppm with 23 of the 24 in the range from 49 to 111 ppm (compared to 36 to 100 ppm in Orgueil pyrrhotites). Thus, pyrrhotites from both of the CI carbonaceous chondrite meteorites we examined have similar Se contents and compositional variability.

The x-ray diffraction patterns for all five IDP particles were similar, displaying diffraction patterns indicative of a mixture of fine and coarse-grained minerals (relative to a 10 micron beam diameter, see Figure 2). The localized diffraction patterns for the coarser grained minerals are consistent with the d-spacings of pyrrhotite. A typical pattern gave spots consistent with one to three pyrrhotite d-spacings. Rotating each particle to a different orientation allowed us to measure other d-spacings in each crystal orientation until at least five different d-spacings were recorded for each Fe-sulfide. These spacings were consistent with pyrrhotite. The powder patterns that were observed, which we believe is produced from a second finer grained mineral, are consistent with the five strongest d-spacings of magnetite, an Fe-oxide which forms of the surfaces of Fe-sulfides due to the heating pulse experienced during atmospheric entry deceleration. Thus, each of the five IDPs we selected is dominated by one or a few large pyrrhotite crystals, and each contains numerous small magnetite crystals consistent with atmospheric entry heating of each particle.

The X-Ray Microprobe was used to measure the Se/Fe ratios in the five IDP pyrrhotites (see Figure 3). We have not measured the Fe contents, but the identification of these particles as pyrrhotite confines the Fe content to a relatively narrow range. The high Se and

Fe contents result in ~2% errors in the Se/Fe ratio, but since the Fe content has not yet been measured there is an ~10% uncertainty in the Se concentrations. Taking the Fe content of the IDP pyrrhotite as 50 wt-%, consistent with the mean Fe content of the Orgueil pyrrhotites, we obtain Se contents of 100, 120, 110, 120, and 90 ppm for the particles L2021D8, L2005P3, L2036G10, L2036I7 and L2036I12, respectively. The average Se content in these five pyrrhotite-dominated IDPs from the stratospheric collectors is ~110 ppm, 1.6 times the mean of ~65 ppm in pyrrhotites from the Orgueil CI carbonaceous chondrite. More significant, however, is the observation that four of the five IDP pyrrhotites have a Se concentration as high as or higher than the highest Se concentration in any of the 20 Orgueil pyrrhotites. Thus, although the number of IDP pyrrhotites we have analyzed is small, due to the scarcity of pyrrhotites on the stratospheric collectors, the results strongly indicate these IDP pyrrhotites are different in Se content from the Orgueil pyrrhotite.

We cannot exclude thermal modification of the pyrrhotite IDPs during atmospheric deceleration. However, the pulse heating of the Orgueil pyrrhotites lowered their Se content relative to Fe [4]. Thus, if the pyrrhotite IDPs experienced thermal modification, the pre-atmospheric Se content would have been higher than the amount we measured, and the difference between IDP pyrrhotites and Orgueil pyrrhotites would be correspondingly greater.

These results indicate that the pyrrhotite-dominated IDPs formed in a region with a higher Se/S ratio than the pyrrhotite in the primitive meteorite Orgueil, or that the IDP pyrrhotite formed at a different temperature than Orgueil pyrrhotite. Either result indicates that IDP pyrrhotites sample a different formation environment than the pyrrhotite crystals in CI carbonaceous chondritic meteorites. Thus, chondritic IDPs differ from meteorites not only in the bulk composition, but also in the element ratios in an individual mineral, pyrrhotite, that is associated with chondritic IDPs. These results are consistent with our prior inferences that chondritic IDPs formed in a different environment than the chondritic meteorites based on the volatile enrichment of IDPs [1]. Keller et al. [6] recently demonstrated that pyrrhotite has a strong absorption feature at ~23.5 micrometers, providing a good match to an absorption feature observed by the Infrared Space Observatory in spectra of regions of circumstellar dust, implying that sulfide grains are an important, previously unrecognized mineral that forms in the region around stars. Further study of IDP sulfides is likely to provide useful insights into the formation of grains early in the history of our Solar System.

Acknowledgements:

NASA Cosmochemistry Grant NAG-5-9393 supported this work. The microdiffraction studies are a collaborative effort between A. Lanzirotti and John Parise (SUNY Stony Brook, Geosciences) to promote

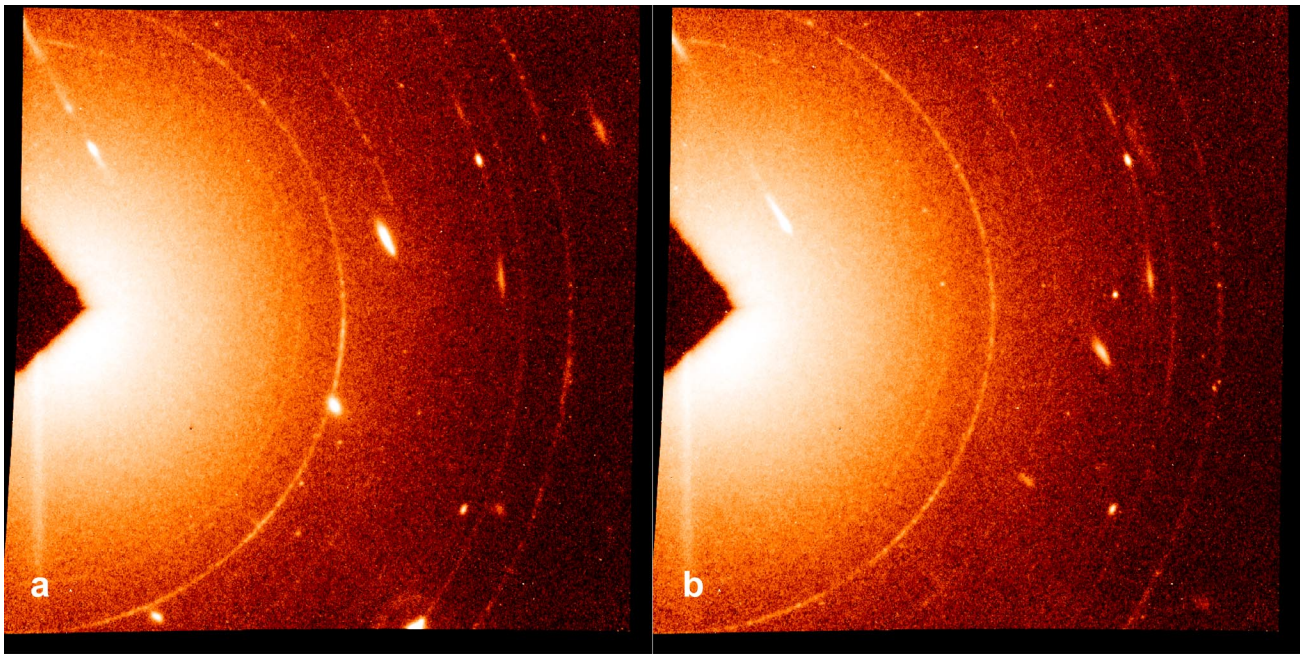

Figure 2. Two X-ray diffraction patterns (a and b) of L2021D8 in slightly different orientations. Bright single point diffraction spots are consistent with the d-spacings of pyrrhotite while the less intense powder patterns are consistent with diffraction from fine-grained magnetite.

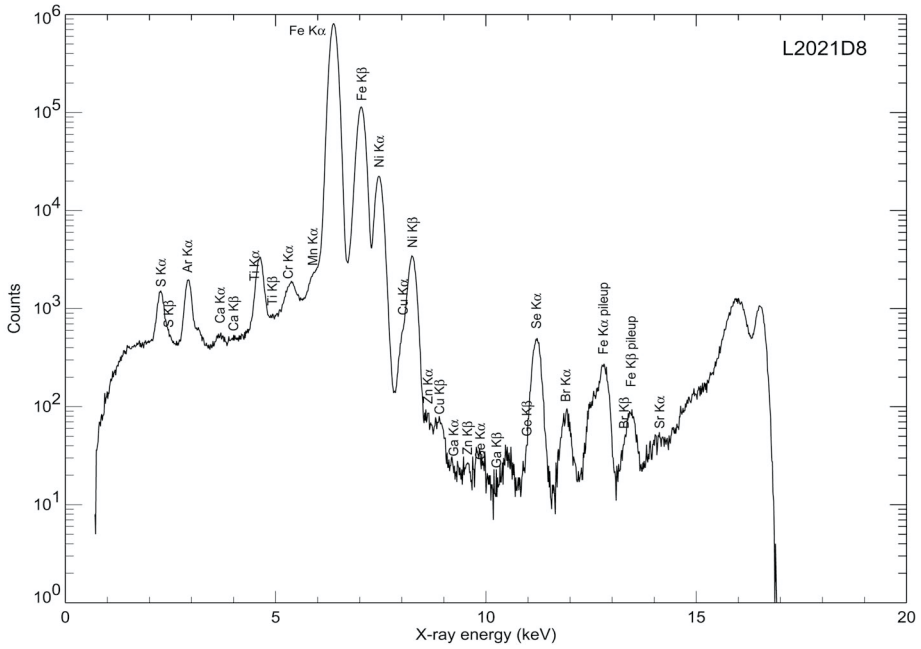

Figure 3. X-ray fluorescence spectrum of L2021D8.

advances in environmental microdiffraction studies at X26A. The installation of the Bruker CCD facility at the NSLS was supported by the NSF through grant EAR-9724501/Stony Brook to John Parise.

References:

[1] G.J. Flynn, "The abundance pattern of elements having low nebular condensation temperatures in interplanetary dust particles: Evidence for a new type of chondritic material," in Physics, Chemistry and Dynamics of Interplanetary Dust, ASP Conf. Series, **104**, p. 291-294, Ast. Soc. of the Pacific Press, 1996.

[2] G. Dreibus, et al., "Sulfur and selenium in chondritic meteorites", *Meteoritics*, **30**, p. 439-445, 1995.

[3] G.J. Flynn and S.R. Sutton, "Cosmic dust particle densities: Evidence for two populations of stony micrometeorites," Proc. Lunar and Planet. Sci, **21st**, p. 541-547, 1990.

[4] A. Greshake, et al., "Heating experiments simulating atmospheric entry heating of micrometeorites," Meteoritics & Planetary Science, **33**, p. 247-290, 1998.

[5] P.J. Eng, M. Newville, M.L. Rivers, and S.R. Sutton, "Dynamically figured Kirkpatrick Baez micro-focusing optics," in X-Ray Microfocusing: Applications and Technique, I. McNulty, ed., Proceedings SPIE, **3449**, p. 145, 1998.

[6] L.P. Keller, et al., "Sulfides in Interplanetary Dust Particles: A Possible Match to the 23 μm Feature Detected By The Infrared Space Observatory," Lunar and Planetary Science XXXI, Abstract #1860, 2000.